Using Spectral Methods to Obtain Particle Size Information from Optical Data: Applications to Measurements from CARES 2010

Dean B. Atkinson[1], Mikhail Pekour[2], Duli Chand[2], James G. Radney[1,***], Katheryn R. Kolesar[5,*], Qi Zhang[3], Ari Setyan[3,**], Norman T. O'Neill[4], Christopher D. Cappa[5]

[1] [Department of Chemistry, Portland State University, Portland, OR, USA, 97207]
[2] [Pacific Northwest National Laboratory, Richland, WA, USA, 99352]
[3] [Department of Environmental Toxicology, University of California, Davis, CA, USA, 95616]
[4] [Centre d'Applications et de Recherches en Télédétection, Université de Sherbrooke, Sherbrooke, Canada]
[5] [Department of Civil and Environmental Engineering, University of California, Davis, CA, USA, 95616]
[*] Now at: Air Sciences, Inc., Portland, OR, 97214, USA
[**] Now at: Empa, Swiss Federal Laboratories for Materials Science and Technology, 8600 Dübendorf, Switzerland
[***] Now at: Material Measurement Laboratory, National Institute of Standards and Technology, Gaithersburg, Maryland, 20899, USA
Correspondence to: D. B. Atkinson (atkinsond@pdx.edu)

Abstract

Multi-wavelength *in situ* aerosol extinction, absorption and scattering measurements made at two ground sites during the 2010 Carbonaceous Aerosols and Radiative Effects Study (CARES) are analyzed using a spectral deconvolution method that allows extraction of particle size-related information, including the fraction of extinction produced by the fine mode particles and the effective radius of the fine mode. The spectral deconvolution method is typically applied to analysis of remote sensing measurements. Here, its application to *in situ* measurements allows for comparison with more direct measurement methods and validation of the retrieval approach. Overall, the retrieved fine mode fraction and effective radius compare well with other *in situ* measurements, including size distribution measurements and scattering and absorption measurements made separately for PM_1 and PM_{10}, although there were some periods during which the different methods yielded different results. One key contributor to differences between the results obtained is the alternative, spectrally based definition of "fine" and "coarse" mode from the optical methods, relative to instruments that use a physically defined cut-point. These results indicate that for campaigns where size, composition, and multi-wavelength optical property measurements are made, comparison of the results can result in closure or can identify unusual circumstances. The comparison here also demonstrates that *in situ* multi-

wavelength optical property measurements can be used to determine information about particle size distributions in situations where direct size distribution measurements are not available.

Introduction

Aerosols remain a substantial source of uncertainty in climate models, despite considerable progress in scientific understanding of their chemical, physical and optical properties in the last few decades (IPCC, 2013). As greater understanding has developed in each of these areas, new complexity is also uncovered and the interconnectedness of the various properties becomes even more evident. Light scattering by atmospheric particles has a net cooling effect on climate that is one major offset to greenhouse gas induced climate warming (Charlson et al., 2005; Bond et al., 2011). The efficiency with which the atmospheric aerosol interacts with electromagnetic radiation (e.g. sunlight) is dependent upon the size, composition, shape and morphology of the particles. These properties are not static in time, instead evolving as particles are transported through the atmosphere as a result of chemical processing, scavenging and changes in the environmental conditions (e.g. relative humidity and temperature) (Doran et al., 2007; George and Abbatt, 2010; Lack and Cappa, 2010).

Characterization of the spatial distribution of aerosol particle concentrations and properties is important to assessing their impact on the atmospheric radiation budget through direct aerosol-radiation and indirect aerosol-cloud interactions. Aerosol optical properties can be measured directly in the laboratory and in the field using both in situ methods (Andrews et al., 2004; Moosmuller et al., 2009; Coen et al., 2013) and remote sensing instruments/platforms, such as sunphotometers and satellites (Holben et al., 1998; Anderson et al., 2005). Alternatively, aerosol optical properties can be inferred from measurements of particle composition, abundance and size distributions (Atkinson et al., 2015). One particular advantage of the remote sensing instruments is that they allow for characterization of column-average atmospheric particle burdens and properties over a large spatial scale and are free from sampling biases as the particles are characterized as they exist in the atmosphere. However, they can only reliably retrieve aerosol properties under cloud-free conditions, and determination of properties beyond the aerosol optical depth (such as the single scatter albedo or the aerosol size distribution) typically requires a data 'inversion' process that relies on an assessment of the wavelength-dependent light attenuation and scattering (Dubovik and King, 2000). *In situ* methods can allow for more detailed characterization of aerosols, including the relationships between size, composition and optical properties, but typically at the expense of reduced spatial coverage and with long-term measurements typically restricted to the surface (Andrews et al., 2004). Given the wide-spread use of aerosol remote sensing and the extensive availability of the data (in particular from ground-based sunphotometer networks such as AERONET and AEROCAN (Holben et al., 1998; Bokoye et al., 2001)), continued

assessment and validation of the inversion methods by comparison with measurements by *in situ* methods is important.

Multi-wavelength optical measurements can yield information about the aerosol size distribution, a principle that dates back to Ångström's observation that the wavelength-dependence of light attenuation by particles was weaker for larger particles (diameters of hundreds of nanometers to micrometers) than for smaller particles (Ångström, 1929). One of the simplest ways of characterizing the wavelength-dependence of optical measurements (whether extinction, scattering or absorption) is through the Angstrom exponent. For a pair of optical measurements at different wavelengths, å $= -\log(b_{x,\lambda 1}/b_{x,\lambda 2})/\log(\lambda_1/\lambda_2)$, where $b_{x,\lambda}$ is the optical coefficient at one of the wavelengths λ; for scattering and extinction å typically increases as particle size decreases. The dependence of b_x on wavelength can alternatively be obtained from a $\log(b_{x,\lambda})$ vs. $\log(\lambda)$ plot using two or more wavelengths; if the dependence is linear, a regression would obtain the same value as the pair-wise treatment, but non-linearity can be accommodated by using the continuous derivative $\alpha = -d\ln(b_{x,\lambda}) / d\ln(\lambda)$ at a specified wavelength. A list of the symbols and acronyms used in this work is provided in Appendix A. The two-wavelength version will be referred to here as the Ångström exponent and the multi-wavelength variant as the spectral derivative. Particle size classification schemes have been proposed (Clarke and Kapustin, 2010) and supported/validated (Eck et al., 2008; Massoli et al., 2009; Cappa et al., 2016) based on the Ångström exponent of extinction or scattering. When observations are made at more than two wavelengths (ideally, widely spaced), further information regarding the nature of the particle size distribution can be extracted. For example, an additional level of refinement of wavelength-dependent measurements of aerosol optical depth (path integrated extinction) was introduced by O'Neill et al. (2005) to aid in the interpretation of the data obtained by the ground-based sunphotometer networks AERONET and AEROCAN. Specifically, O'Neill et al. (2003; 2005) showed that the fine mode fraction (FMF) of extinction and the fine mode effective radius, $R_{eff,f}$ could be extracted directly from the multi-wavelength optical depth or extinction measurements available from remote sensing. The FMF provides for an approximate discrimination between what are typically naturally produced coarse mode particles (dust or sea spray) and what are often anthropogenically associated fine mode particles. Thus, parameters such as the FMF can provide a nominal indication of the relative contributions of natural versus anthropogenic particles to the atmospheric AOD. Variations in $R_{eff,f}$ provide information on the sources of the fine mode particles - as different sources yield fine mode

particles with different size distributions - or the extent to which particles have undergone atmospheric processing, which can change the size distribution (and chemical composition) in systematic ways.

In the spectral curvature approach of O'Neill et al. (2003), the fine mode spectral derivatives (α_f = first derivative and α_f' = second) and the FMF are first extracted from multi-wavelength extinction data using a process described as Spectral Deconvolution. The fine mode spectral derivatives can then be used to obtain the fine mode effective radius from a fine mode spectral curvature algorithm. Alternatively, the fine mode effective radius can be calculated from direct measurements of size distribution (e.g. from scanning mobility particle sizer) using equation 1 (Hansen and Travis, 1974):

$$R_{eff,f} = \frac{\int_0^\infty R\pi R^2 \frac{dN}{dlnR} dlnR}{\int_0^\infty \pi R^2 \frac{dN}{dlnR} dlnR} \quad (1)$$

where *R* is the particle geometrical radius and dN/dlnR is a number weighted size distribution for which $R_{eff,f}$ is the first moment (average radius) of the surface-area weighted size distribution. $R_{\mathrm{eff,f}}$ is an effective radius that characterizes, approximately, the average size of particles in the fine mode that scatter solar radiation. In this work, we compare the optically obtained $R_{eff,f}$ retrievals to those calculated by numerically evaluating the integrals of Equation 1 using the observed size distributions produced by scanning mobility particle sizers. A single log-translatable particle size distribution (i.e., a PSD that can be translated along the log-transformed particle size axis without changing the form of the distribution function) is, in many cases, a reasonable representation of the size distribution of observed aerosol fine modes (O'Neill et al., 2005). In these cases, the fine mode can be characterized by the single parameter $R_{eff,f}$ facilitating comparisons and examination of trends in sources and/or atmospheric processing.

Numerical methods such as those developed by O'Neill et al. (2003) were originally applied to remote sensing measurements, but can also be applied to *in situ* extinction measurements. Beyond adding to the utility of the *in situ* optical measurements, this provides an opportunity to test the methods against other, complementary measures of particle size and size-dependent scattering and extinction. For example, Atkinson et al. (2010) used the approach of O'Neill et al. (2003) to analyze *in situ,* three-wavelength aerosol extinction measurements made during the 2006 TexAQS II campaign near Houston, TX. More recently, Kaku et al. (2014) showed, for a range of marine atmospheres, that the application of this spectral approach to obtain FMF from three-wavelength scattering coefficient measurements was largely coherent with the sub-micron fraction of scattering (SMF), obtained from scattering coefficient measurements of the fine and coarse mode components using impactor-based separation of the

aerosol. These studies, and others, provide a useful basis for understanding the accuracy and applicability of the parameters retrieved from remote sensing data. However, further assessment in a wide range of environments is necessary given that networks employing such spectral remote sensing algorithms (AERONET and some surface based sites) represent locations impacted by particles from diverse sources.

In this work, measurements of aerosol optical properties (extinction, scattering and absorption coefficients) made at multiple wavelengths during the 2010 Carbonaceous Aerosols and Radiative Effects Study (Fast et al., 2012; Zaveri et al., 2012) are reported and analyzed using the O'Neill et al. (2003) and the O'Neill et al. (2008b) methods. The measurements were made at two locations near Sacramento: a more urban site in Granite Bay, CA (T0) and a more rural site in Cool, CA (T1) that were often linked by direct atmospheric transport. The multi-wavelength measurements were made using three types of optical instruments (specifically seven separate instruments at the two locations). The multi-wavelength measurements of the extinction coefficients (either measured directly or produced from the sum of scattering and absorption coefficients) are used to retrieve the fine mode fraction of extinction and fine mode effective radius. These results from the retrieval, described in more detail in the next section, are compared to other, complementary *in situ* measurements. Scattering and absorption coefficients were measured after aerodynamic separation into the PM_1 and PM_{10} fractions, which allowed the sub-micron fraction (SMF) of extinction to be directly determined. The *in situ* SMF can be compared with the FMF from the spectral retrieval method. In this work, sub-micron particles are those with nominal aerodynamic diameters ($d_{p,a}$) smaller than 1 µm, likely resulting in geometric diameters below 800 nm. Also, size distribution measurements allowed for determination of the fine-mode effective radii (via Eqn. 1), which are compared with those obtained from the spectral retrieval.

Theoretical Approach

The Spectral Deconvolution Algorithm with Fine Mode Curvature (SDA-FMC) Approach

This section provides a qualitative description of the fine and coarse mode AOD (or extinction) retrieval algorithm (SDA, or spectral deconvolution algorithm) and fine mode optical sizing (FMC or fine mode curvature) method developed by O'Neill. The details of the derivation and application of the SDA are provided in previous publications (O'Neill et al., 2003; Atkinson et al., 2010; Kaku et al., 2014). The MATLAB code that implements the approach is available from O'Neill upon request. Application of both approaches requires a robust set of measurements of aerosol optical extinction or scattering (or optical

depth) at a minimum of three wavelengths that should be widely spread across the optical region of the spectrum (near UV through the visible to the near IR; see, for example, O'Neill et al. (2008a)).

The fundamental assumption of the SDA approach is that most ambient aerosol size distributions are composed of two optically-relevant modes: a fine mode having an effective radius (and to a lesser extent, geometric standard deviation) that is a function of atmospheric processing, and a separate coarse mode, largely in the supermicron ($d_{p,a}$ > 1 μm) size range. A common assumption is that the fine mode is more closely associated with anthropogenic activities and the coarse mode with natural sources, although this can be somewhat confounded by smoke from biomass burning (Hamill et al., 2016). In particular, it can be difficult to distinguish biomass burning particles from particles derived from urban sources, as both primarily fall within the fine mode and are somewhat absorbing. The FMC (Fine Mode Curvature) algorithm employs the fine mode optical parameters retrieved using the SDA to estimate both a fundamental indicator of optical particle size (the fine mode van de Hulst parameter) and from this, an indicator of microphysical particle size (the fine mode effective radius); these are both defined below.

Spectral deconvolution of the fine and coarse mode extinction and derivation of the fine mode spectral derivatives (SDA)

The spectral deconvolution algorithm begins by isolating the fraction of total extinction due to particles in the fine mode, based on the stronger dependence of the extinction (scattering)[1] on wavelength for smaller particles. Current applications of the method start by fitting ln(b_{ext}) (or ln(b_{scat}) or ln(AOD)) versus ln(λ) to a second order polynomial, where b_{ext} is the measured wavelength-dependent extinction coefficient (see Atkinson et al. (2010) and Kaku et al. (2014) for scattering and extinction coefficient applications, Saha et al. (2010) for a sunphotometry AOD application and Baibakov et al. (2015) for a starphotometry AOD application). The extinction and its first and second derivatives are determined from the fit at a reference wavelength of 500 nm, a common reference wavelength along with 550 nm in optical studies. The first derivative (i.e. slope) is denoted α in analogy to the Ångström exponent, but in this non-linear, second order approach it is a function of wavelength. The second derivative α' (i.e. spectral curvature) may, in principle, be wavelength dependent over the observed range, but using a second order polynomial fit yields a constant value. Values of α and α' associated with the fine mode

[1] We will stop inserting "(scattering)" at this point although all references below should be understood to apply to both scattering and extinction.

and the coarse mode are indicated using subscript f or c, respectively. In this work, only a second order fit is possible because only three measurements are used to define the wavelength dependence. In the SDA-FMC approach, the observed spectral derivative (α) is used along with the SDA-derived fine mode spectral derivative (α_f) to produce the fine mode fraction of extinction (FMF), given as:

$$FMF = \frac{\alpha - \alpha_c}{\alpha_f + \alpha_c} \quad (2)$$

Ultimately, the fine mode slope and curvature are both used in the FMC algorithm to determine the fine mode effective radius (discussed in the next section).

The algorithm proscribes constant values of the spectral slope and curvature for all coarse mode aerosols (α_C and α'_C) at the reference wavelength of 500 nm. Specifically, α_C = -0.15±0.15 and α'_C = 0.0±0.15, with the uncertainties as per O'Neill et al. (2003). O'Neill et al. (2001) showed that an assumption of an aerosol size distribution with two distinct modes yields a series of three equations that express the relationships between the observed parameters (AOD or extinction coefficient, α, α') and their fine and coarse mode analogues. Specifically, the equations can be inverted to yield the fine mode spectral derivative, the fine mode curvature (α_f') and the fine and coarse mode AOD or b_{ext} values. It should be noted that the fitting of a 2nd order polynomial to input AOD or b_{ext} spectra is only an approximation relative to a higher order polynomial. The use of a 2nd order polynomial represents a compromise between higher order spectral polynomials being better representations of theoretical Mie spectra and the beneficial damping effects of lower order polynomials in the presence of noisy spectra (O'Neill et al., 2001). The observationally determined total and fine mode spectral derivative and proscribed coarse mode spectral derivative are then used to calculate the fine mode fraction of extinction at the reference wavelength (here 500 nm) using Eqn. 2.

Estimation of the Fine Mode Effective Radius – the Fine Mode Curvature (FMC) approach

Using the SDA-derived, fine mode spectral derivatives (α_f' and α_f), an estimate of the fine mode effective radius is obtained. The basis for this approach is a fundamental parameterization involving the effective van de Hulst phase shift parameter for fine mode aerosols and its representation in α_f' versus α_f space.

Full details are provided in O'Neill et al. (2005) and O'Neill et al. (2008b), and only a summary of the parameterization is provided here. The van de Hulst parameter for the fine mode, *ρeff,f*, is given by:

$$\rho_{eff,f} = 2 * \frac{2\pi R_{eff,f}}{\lambda} |m - 1| \quad (3)$$

where λ is the reference wavelength and m is the complex refractive index at that wavelength (O'Neill et al., 2005). An estimate of this purely optical parameter is based on a 3rd order polynomial derived from numerical Mie simulations that relate $\rho_{eff,f}$ and the polar angle (ψ) coordinate of any point in α_f' vs. α_f space (O'Neill et al., 2005). The value of ψ for any given retrieval is simply the arctangent of α_f' divided by α_f (minus small prescribed offsets of $\alpha_{f,0}'$ over $\alpha_{f,0}$ respectively). Individual simulated contour curves of α_f' versus α_f correspond to particle size distributions of differing $R_{eff,f}$ for constant values of refractive index and were illustrated in Figure 1 of O'Neill et al. (2005). The three different "lines of constant $\rho_{eff,f}$" in that figure correspond to three different values of ψ (where both $\rho_{eff,f}$ and ψ increase in the counterclockwise direction from the horizontal). The $R_{eff,f}$ value are then computed from the retrieved value of $\rho_{eff,f}$, by inverting equation (3), if the refractive index of the particles is known. Since the refractive index is generally unknown for the situations we consider here, the information provided by this approach is actually a combination of size and composition. In many cases, an average, constant value for the real portion of the refractive index can be assumed and the imaginary part neglected to provide an estimate of the effective radius; this is, in part, because the imaginary component is typically much smaller than the real component of the refractive index, and thus the $R_{eff,f}$ value is relatively insensitive to variations in the imaginary component. This treatment is questionable if strong changes in the average composition that lead to changes in m are suspected. For example if the composition shifted from pure sulfate aerosol (m = 1.53 + 0i) to a brown carbon organic (m = 1.4 + 0.03i) this would introduce a 33% shift in the derived radius with no change in actual size; the majority of this shift in the derived radius results from the change in the real component of the refractive index.

The FMC method represented by the inversion of equation (3) has been less rigorously validated than the SDA portion and is expected to be more susceptible to problems related to measurement errors and a decreasing sensitivity with decreasing fine mode fraction of extinction. The FMC validation is largely confined to comparisons with the more comprehensive AERONET inversions of Dubovik and King (2000), referred to henceforth as the D&K inversions. These inversions, which require the combination of AOD and sky radiance data, are of a significantly lower frequency than simple AOD measurements. The sky radiance data are collected nominally once per hour while AOD measurements are made once every 3

minutes. Comparisons between the FMC method and the D&K inversions show averaged FMC versus AERONET differences of 10% ± 30% (mean ± standard deviation of ($\rho_{eff,f,FMC}$ - $\rho_{eff,f,D\&K}$) / $\rho_{eff,f,D\&K}$) for large FMF values > 0.5, at least for the limited data set of O'Neill et al. (2005) and confirmed by more recently unpublished AERONET-wide comparisons between the FMC and D&K methods.

Application of the SDA-FMC method to in situ extinction measurements

This paper seeks to address the following two key questions pertaining to the use of the SDA-FMC algorithm with extinction measurements, especially those produced by the cavity ring-down instruments, to extract information about aerosol size, both the partitioning of the extinction between the fine and coarse modes and the extraction of a single parameter size characterization of the fine mode.

1.) Can the approach be used reliably to extract the fine and coarse mode fractions of the extinction in situations where only a single optical instrument is used?

and,

2.) In situations where complementary measurements (mobility-based sizers, parallel or switching nephelometers, etc.) are available, what information can be determined from the comparison of the products of the SDA-FMC approach to comparable information obtained in other ways?

It has been suggested that a single multi-wavelength optical measurement of the fine mode fraction could be less expensive than derivation of the sub-micron fraction of scattering using parallel nephelometers (Kaku et al., 2014). The use of two size-selected inlets (e.g., 1 and 10 µm cyclones) and parallel nephelometers is not prohibitively expensive, but the typical concerns regarding calibration maintenance and careful and consistent application of correction factors for truncation angle and non-Lambertian illumination can be magnified when measurements are combined (either as differences or ratios) since systematic errors may not undergo partial cancellation like random errors.

In principle, the use of two parallel CRD extinction measurements could mitigate some of the possible errors with parallel nephelometers. Cavity ring-down measurements directly quantify total extinction within the cavity, which is contributed from both gases and particles (Smith and Atkinson, 2001; Brown, 2003). To determine extinction by aerosols only, the entering air stream is periodically directed through a filter such that a gas-only reference is determined. Extinction by aerosol particles is determined relative to this gas zero. The aerosol extinction is further corrected to account for the practical aspect

that the complete mirror-to-mirror distance of the optical cavity is typically not filled with aerosols (to keep the mirrors clean) (Langridge et al., 2011). The former (zeroing) limits instrument precision and sometimes accuracy while the latter (path length) limits instrument accuracy. In general these procedures are identical for the two parallel instruments and are very stable in time, so they would only be expected to produce a small and consistent bias. To our knowledge, currently no single-package, multi-wavelength direct extinction (cavity-enhanced) instruments are commercially available. Multiple single-wavelength instruments operating at different wavelengths could be deployed, but might be prohibitively expensive.

For detailed knowledge of the fine mode size distribution, the use of scanning mobility analyzer-based sizing instruments is preferable since the full mobility size distribution is obtained, as opposed to only the effective radius provided by the FMC procedure. However, scanning mobility sizer instruments typically have maximum diameters of only 700 to 800 nm, and both scanning and multi-channel variants are of comparable expense and complexity as CRD instruments. In order to obtain additional information about the coarse mode size distribution and contribution to the optical effects, an aerosol particle spectrometer (APS) is generally added to the measurement suite.

The purely spectrally-based mode separation inherent in the SDA obviates the need for a physical cut point selection, such as that required to measure the PM_1 scattering product used in this work. This can be advantageous, since selection and maintenance of a size cut-point is a possible source of differences between some measurements (and variability of all measurements using physical separation) of the sub-micron fraction (SMF) of scattering, absorption or extinction. The SMF is fundamentally different from the FMF, although both provide an indication of the fractional optical contribution of smaller particles. In fact, there are fundamental differences between many of the SMF or FMF data products that are currently available. For example, the Dubovik and King (2000) SMF data product tries to locate the separation radius (called the inflection point) at a minimum of the particle size distribution obtained from the inversion procedure. This results in a variable cut point that can be interpreted as assigning a portion of the coarse mode to the fine mode (O'Neill et al., 2003). The aerodynamic diameter selected for the physical separation used in the SMF presented in this work might result in some mis-assignment of fine mode extinction to the coarse mode, since (i) the aerodynamic separation results in a cut point that is less than 1 μm geometric diameter and (ii) the cut point might not correspond to a local minimum of the size distribution. These definitional differences should be kept in mind when comparing fine mode apportionments (SMF or FMF) from different measurements/data treatments. And all of

these data products will usually differ significantly from the optical properties of the $PM_{2.5}$ fraction used to define the fine mode for air quality regulations and to exclude larger particles in the CRD instruments at T0. The latter allowed a significant fraction, but not all of the optically coarse particles into the instruments, as shown in the Results section. For the comparisons presented in this work, in cases where there is significant penetration of one of the modes into the size regime defined by the physical cut-point as the other mode (or significant overlap of two or more size modes) there are noticeable differences between the physically-defined SMF and the FMF produced by the SDA.

Experimental

The instrument suites used, sampling conditions and methodology and goals of the CARES study have been summarized by Zaveri et al. (2012). A summary of the instrumentation used to make the light extinction, scattering and absorption measurements is provided in Table 1. Extinction was measured either directly (using cavity ringdown spectroscopy) or as the sum of scattering and absorption. A brief description of the key instruments used in the current analyses is given below.

Table 1: Summary of optical instruments used at the T0 and T1 sites

Property	Instrument	Wavelength	Size Cut*
		T0	
Extinction	UCD CRD	405, 532 nm	2.5 μm
	PSU CRD	532, 1064 nm	2.5 μm
Scattering	PNNL Nephelometer	450, 550, 700 nm	1 μm, 10 μm
Absorption	PNNL PSAP	470, 522, 660 nm	1 μm, 10 μm
		T1	
Extinction	PSU CRD	355, 532, 1064 nm	None applied
Scattering	PNNL Nephelometer	450, 550, 700 nm	1 μm, 10 μm
Absorption	PNNL PSAP	470, 522, 660 nm	1 μm, 10 μm

*For the entries with two size cuts listed, the sampling system switched between the two on a 6 minute cycle

Instruments used at the T0 site (American River College, Granite Bay, CA USA)

Cavity Ring-down Extinction: The b_{ext} measurements at 405 nm and 532 nm were made using the UC Davis two-wavelength Cavity Ring Down-Photoacoustic Spectrometer (CRD-PAS) instrument (Langridge et al., 2011; Lack et al., 2012). Full details of these measurements are available in Cappa et al. (2016) and Atkinson et al. (2015). These measurements were only made for a subset of the CARES campaign, from 20:00 PDT on 16 June through 09:00 PDT on 29 June. At 532 nm, b_{ext} was measured at low (~25%), mid

(~75%) and high (~85%) relatively humidity. At 405 nm only low RH measurements were made, and so only the low RH 532 nm measurements are used in this study. The CRD-PAS sampled behind a $PM_{2.5}$ (aerodynamic diameter <2.5 μm) URG Teflon-coated aluminum cyclone. A separate CRD instrument deployed by the PSU group at T0 used a single optical cavity to measure the sub-2.5 μm (sampled through a similar URG cyclone) aerosol extinction coefficient at 532 and 1064 nm simultaneously (Radney et al., 2009). This instrument did not incorporate intentional RH control, but efforts were made to maintain nearly ambient conditions, resulting in low RH (25 - 40 %) throughout most of the campaign, as measured by an integrated RH/T sensor (Vaisala HMP70). Daytime ambient RH was similar to the low RH value during the CARES campaign (Fast et al., 2012).

To obtain three-wavelength b_{ext} measurements for use in the SDA-FMC analysis, we combined the measurements from the two CRD instruments (the 1064 nm measurements from the PSU instrument were used with the 532 nm and 405 nm UCD data after all had been averaged to one-hour). To assess whether this was a reasonable approach, the 532 nm time series data from the two instruments were overlaid and examined for differences. There is a high degree of temporal correspondence between the measurements from the two instruments, although there was a clear difference in precision, with the UCD CRD having approximately 3 times better precision than the PSU instrument at comparable integration times. This difference in precision results from differences in instrumental design and (likely) mirror quality. A scatterplot (Figure S1) of $b_{ext,PSU}$ versus $b_{ext,UCD}$ also showed good correlation, with a best fit line from an orthogonal distance regression fit having a slope = 0.96 and an intercept that was statistically indistinguishable from zero. This is within the uncertainties of the instruments. The good agreement at 532 nm between the PSU and UCD instruments suggests that combining the 1064 nm measurements from PSU with the 405 nm and 532 nm measurements from UCD is reasonable. If the very slight low bias in the 532 nm b_{ext} from PSU relative to the UCD measurements applies to the 1064 nm measurements then the derived FMF values might be slightly overestimated.

Size-selected absorption and scattering (nephelometer and PSAP): The low RH scattering and absorption coefficients were alternatingly measured for PM_{10} and PM_1 aerodynamic size selected aerosol using the PNNL Aerosol Monitoring System, a clone of NOAA/CMDL's Aerosol Monitoring System (detailed description at http://www.esrl.noaa.gov/gmd/aero/instrumentation/instrum.html and in Zaveri et al. (2012)). The relevant measurements are: light absorption coefficients at three-wavelengths (Radiance Research Particle Soot Absorption Photometer [PSAP]) and total scattering coefficients (three-wavelength nephelometer, TSI 3563). The scattering coefficients were corrected for truncation error

(Anderson and Ogren, 1998) and the absorption coefficients for filter effects (Ogren, 2010). The absorption coefficients were interpolated to the nephelometer wavelengths assuming the inverse wavelength dependence characteristic of uncoated black carbon, as appropriate for this region (Cappa et al., 2016). The absorption and scattering coefficients for PM_1 or PM_{10} are then summed after averaging to one-hour intervals and using the mean of the 450 and 550 nm values to obtain b_{ext}(500 nm). The extinction fraction of the PM_1 (herein, the SMF) at the visible wavelength (500 nm) is then calculated from their ratio

$$SMF_{ext} = \frac{b_{ext,PM1}}{b_{ext,PM10}} \quad (4)$$

Particle size control was effected by 2 impactors (1 µm and 10 µm) upstream of the PSAP and nephelometer. The 10- µm impactor was always present in the sampling line, and the flow was switched to run through the 1- µm impactor on 6-min intervals, yielding alternating 6-min measurements of submicron and coarse (< 10 µm) particle modes.

Fine particle size distribution: The submicron dry particle mobility diameter ($d_{p,m}$) size distribution (12 nm to 737 nm) was measured using a scanning mobility particle sizer (SMPS) comprised of a charge neutralizer, differential mobility analyzer and condensation particle counter (TSI 3081 DMA column and model 3775 CPC). The SMPS data were corrected for multiply-charged particles and diffusional losses. These size distribution measurements are used to calculate $R_{eff,f}$ values from Eqn. 1, which will be referred to as $R_{eff,f,size}$. It should be noted that a mobility diameter of 737 nm corresponds to an aerodynamic diameter of 919 nm (assuming a density of 1.5 g cm^{-3}, a reasonable value for the campaign based on the observed particle composition (Atkinson et al., 2015)).

Instruments used at the T1 site (Evergreen School, Cool, CA USA)

Cavity Ring-down Extinction: The PSU group deployed a custom CRD instrument that used separate optical cavities to measure b_{ext} at 355 nm, 532 nm, and 1064 nm simultaneously in each of four separate flow systems that were intended to measure total and submicron aerosol and submicron aerosol that had been conditioned to have elevated and suppressed RH. Only the total aerosol flow results are used here as this prototype system suffered from signal to noise problems and RH/temperature control issues. As with the T0 PSU instrument, the total aerosol system attempts to measure particle extinction at nearly ambient conditions, resulting in low RH (25 – 40 %) throughout most of the campaign, as

388 measured by an integrated RH/T sensor (Vaisala HMP70). No intentional size cut was applied to these
389 measurements, although the system was not optimized for transmission of coarse mode particles.

390 Size-selected absorption and scattering (Nephelometer and PSAP): An identical instrument suite to that
391 used at T0 was deployed and the same data analysis was conducted.

392 Fine particle size distribution: The SMPS used at T1 is a similar design described in (Setyan et al., 2012)
393 and it measured low RH particle sizes from 10 nm to 858 nm. The SMPS data were corrected to take into
394 account the DMA transfer function, the bipolar charge distribution, the CPC efficiency and the internal
395 diffusion losses (Setyan et al., 2014).

396 ***Uncertainties in the derived and measured values***

397 The uncertainty in the SMF has been estimated from standard error propagation of the uncertainties in
398 the PM_1 and PM_{10} extinction measurements. The assumed uncertainties in $b_{ext,PM1}$ and $b_{ext,PM10}$ are ±1
399 Mm^{-1}. This uncertainty estimate accounts only for random errors, not systematic errors.

400 Uncertainties in the FMF have been estimated based on the uncertainties in the inputs to the SDA-FMC
401 procedure, namely the b_{ext} values. The assumed uncertainties in the input b_{ext} were instrument specific:
402 <1 Mm^{-1} for the UCD CRD, 1 Mm^{-1} for the nephelometer plus PSAP and PSU CRD at T0, and 3 Mm^{-1} for
403 the PSU CRD at T1. The input uncertainties are propagated through the various mathematical
404 relationships using standard methods. The FMF error estimate includes some of the factors that
405 contribute systematic uncertainty in the method. As noted in the Theoretical Approach section, FMF
406 values from the SDA-FMC procedure have been shown to agree well with those determined from the
407 more comprehensive inversion method of Dubovik and King (2000).

408 Uncertainties in the derived $R_{eff,f}$ are also estimated from the uncertainties in the input values. The size-
409 distribution derived $R_{eff,f}$ values depend on the SMPS measurements. The SMPS instruments were
410 calibrated (using 200 nm polystyrene latex spheres) prior to the campaign and a drier was used to keep
411 the aerosol RH < 30% throughout the entire campaign. Periodic checks throughout the campaign
412 indicate consistent sizing performance to within 5%. The size distribution data used here were corrected
413 for DMA transfer function, the bipolar charge distribution, the CPC efficiency and internal diffusion
414 losses. Under these conditions the estimated uncertainties for D_p are around 10% for the size range
415 between 20 and 200 nm (Wiedensohler et al., 2012). Although larger uncertainties could exist for
416 smaller and larger particle sizes, the derived $R_{eff,f}$ values fell primarily in this range. The estimated SMPS
417 uncertainty (Wiedensohler et al., 2012) was estimated based on intercomparisons between different

SMPS instruments and thus probably represents both determinate and indeterminate errors. The relative uncertainty in the $R_{eff,f}$ from the size distribution measurement is thus estimated to be 10%. This estimate mainly reflects uncertainties in the absolute size, since there is expected to be significant cancellation in the errors produced by the particle counter (the same data are used in the numerator and denominator of Eq. 1).

Estimating the uncertainty in the $R_{eff,f}$ from the SDA-FMC is more challenging because the uncertainties cannot be simply propagated through the equations. Therefore, an approach was taken wherein a large number of $R_{eff,f}$ values were calculated from input b_{ext} that were independently, randomly varied within one standard deviation of the measured value, assuming a normal distribution of errors. Potential uncertainty or variability in the real refractive index was accounted for based on the compositional variation (Atkinson et al., 2015) and assuming volume mixing applies. The standard deviation (1s) was 0.015. This is likely a lower estimate of the uncertainty in the RI, as it does not account for absolute uncertainty in the estimate. The standard deviation of the derived $R_{eff,f}$ is taken as the uncertainty. This Monte Carlo-style approach does not incorporate systematic error sources. The relative uncertainty in the derived $R_{eff,f}$ is found to range from a few percent up to 40%, depending on the particular instrument suite considered and measurement period. In general, the uncertainties were larger for the PSAP and nephelometer, presumably because the wavelengths used are more closely spaced.

Results and Discussion

Fine mode fraction of extinction

The CRD-based extinction measurements were used to derive the FMF_{ext} using the SDA. This will be referred to as the $FMF_{ext,CRD}$. For the T0 site, the $FMF_{ext,CRD}$ is for $PM_{2.5}$ while at T1 no physical cut point was introduced, so PM_{10} is a reasonable expectation. The time series of the CRD-based b_{ext} values and of the derived $FMF_{ext,CRD}$ at the T0 site are shown in Figure 1 (all times in PDT – local time during the study). The $FMF_{ext,CRD}$ varies from 0.54 to 0.97, with a mean of 0.79 ± 0.1 (1 σ) as summarized in Table 2.

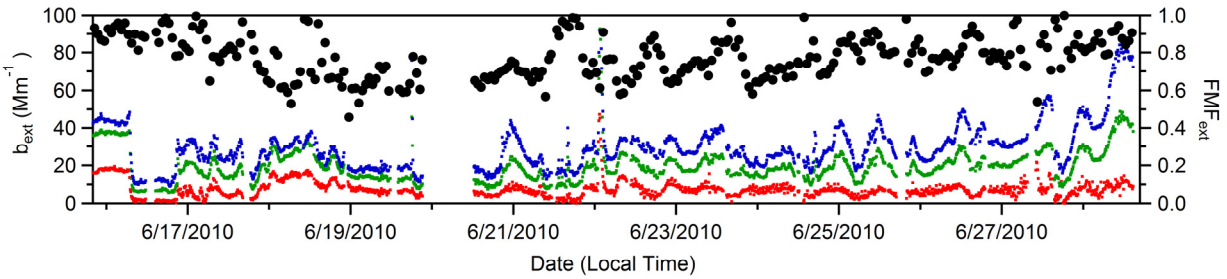

445

446 **Figure 1** – Time series of CRD extinction coefficient observations (left axis) and the derived $FMF_{ext,CRD}$
447 (right axis) at T0 during the time period analyzed in this work. The blue, green and red traces are the
448 405 nm, 532 nm and 1064 nm b_{ext} (respectively) and the black points show the 1 h average $FMF_{ext,CRD}$
449 from the SDA analysis. A $PM_{2.5}$ size cut was applied during the sampling.

450

451 The fine mode fraction of extinction at T0 was alternatively determined from the PM_{10} b_{ext}
452 measurements from the nephelometer and PSAP, referred to as $FMF_{ext,sum}$. The SDA-derived $FMF_{ext,CRD}$
453 and $FMF_{ext,sum}$ values are compared with the sub-micron fraction of extinction determined from the
454 combined PM_1 and PM_{10} nephelometer and PSAP measurements (from the latter part of the campaign)
455 at T0 (Fig. 2). The $FMF_{ext,CRD}$, $FMF_{ext,sum}$ and $SMF_{ext,sum}$ all exhibit the same general temporal dependence.
456 In general, the $FMF_{ext,CRD} > FMF_{ext,sum} \sim SMF_{ext,sum}$ although the specific relationships vary with time. For
457 example, there are periods when the $FMF_{ext,sum}$ and $SMF_{ext,sum}$ are nearly identical (e.g. 20 June – 23
458 June) and periods when the $SMF_{ext,sum}$ is somewhat lower than the $FMF_{ext,sum}$ (e.g. 24 June – 25 June).

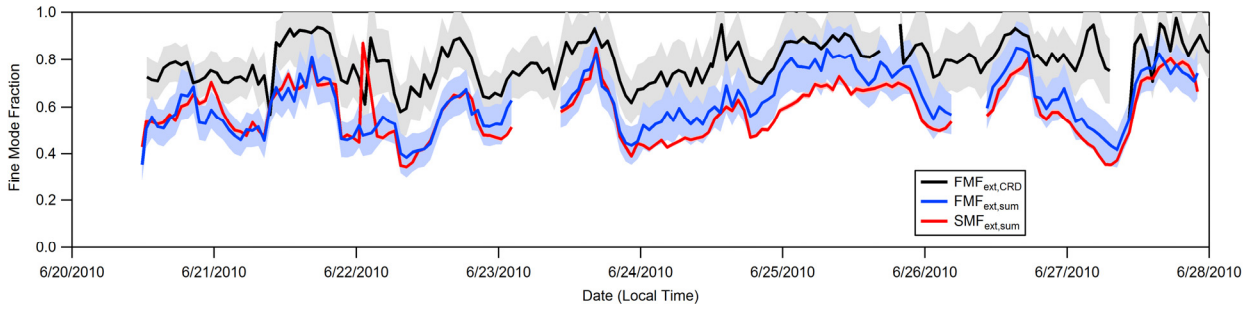

459

460 **Figure 2** – Time series of the fine mode fractions and sub-micron fraction of extinction at T0. The
461 red trace is the $SMF_{ext,sum}$ determined from the $b_{ext}(PM_1) / b_{ext}(PM_{10})$ ratio. The black and blue
462 traces are the FMF_{ext} from the SDA analysis of the CRD extinction (black) and nephelometer +
463 PSAP extinction (blue). The $FMF_{ext,CRD}$ values are the same as those of Fig. 1 for the latter half of
464 the campaign. Uncertainty ranges are shown as light colored bands. The uncertainty of SMF is
465 only slightly wider than the heavy line that was chosen to represent it.

466

467 The $FMF_{ext,CRD}$ was determined for $PM_{2.5}$ while the $FMF_{ext,sum}$ was determined for PM_{10}. If a substantial
468 fraction of the scattering was contributed by particles with diameters >2.5 μm, then the $FMF_{ext,CRD}$

should be larger than the $FMF_{ext,sum}$, as was observed. Kassianov et al. (2012) used measured particle size distributions from CARES to show that supermicron particles contributed significantly to the total scattering, consistent with the observation that $FMF_{ext,CRD} > FMF_{ext,sum}$. Variability in the difference between the $FMF_{ext,CRD}$ and $FMF_{ext,sum}$ likely reflects variability in the contribution of these larger particles to the total scattering.

The $FMF_{ext,CRD}$, $FMF_{ext,sum}$ and $SMF_{ext,sum}$ were similarly determined from the measurements at the T1 site (Figure 3). For T1, the CRD measurements were made for particles without any intentional size cut applied, as opposed to the $PM_{2.5}$ size cut used for the T0 measurements. At this downwind site the $SMF_{ext,sum}$, $FMF_{ext,CRD}$ and $FMF_{ext,sum}$ were all very similar, both in terms of the absolute magnitude and the temporal variability. The $FMF_{ext,CRD}$ ranged from 0.22 to 0.89, with a mean of 0.58 ± 0.16. That the $FMF_{ext,CRD}$ and $FMF_{ext,sum}$ are very similar in absolute magnitude for T1 but differ at T0 (while still exhibiting similar temporal variability) is likely related to the application of an intentional size cut for the CRD measurements at T0 but not at T1. The observations suggest that the T1 CRD without the size cut samples coarse-mode particles with a similar efficiency as the nephelometer and PSAP having the PM_{10} size cut.

Overall, these results indicate that the use of the spectral deconvolution algorithm on optical data can robustly provide information on the fine mode fraction of extinction. Moreover, since the FMF_{ext} results at T1 are similar for the two types of extinction measurements, it seems that the narrower wavelength range of the nephelometer (450, 550, 700 nm) and PSAP (470, 522, 660 nm) compared to the CRD instruments used here is still adequate to define the spectral dependence of extinction for extraction of the slope and curvature parameters. However, the results demonstrate that the optical method does not allow for a precise definition of “fine” and “coarse” in terms of a specific, effective size cut that distinguishes between the two regimes. While the SMF has an explicitly defined size cut (PM_1), the effective size cut for the FMF can vary. The effective size cut is dependent on the shapes (i.e. widths, positions and number of actual modes) of the size distributions in the “fine” and “coarse” size regimes and the extent of overlap between them, which is dependent on the size range of particles sampled (e.g. $PM_{2.5}$ versus PM_{10}). For remote sensing measurements, the particular size that distinguishes between the fine and coarse mode therefore likely varies between locations and seasons. Nonetheless, since the major sources of fine and coarse mode particles are likely to be reasonably distinct in many environments, the $FMF_{ext,CRD}$ provides a reasonable characterization of the variability in the

contributions of such sources to the total extinction and, in environments where the extinction is dominated by scattering (i.e. when the SSA is large), to the total scattering as well.

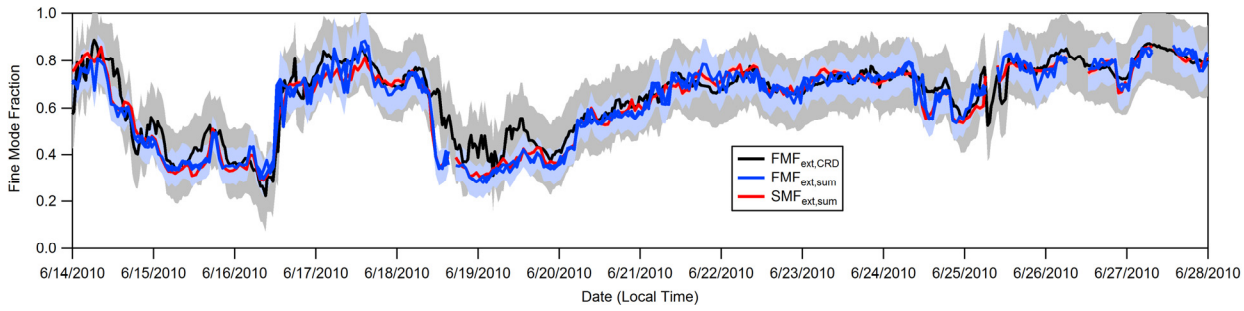

Figure 3 – the fine mode fraction of extinction (SMF and FMF_{ext}) for the latter half of the campaign at T1. Here, the $FMF_{ext,CRD}$ is determined for particles sampled without a size cut applied. Uncertainty ranges are shown as light colored bands.

Effective fine mode radius product of SDA-FMC

The SDA-FMC analysis also allows for derivation of the fine mode effective radius, $R_{eff,f}$, via Eq. 3. Determination of $R_{eff,f}$ requires knowledge of the real and imaginary parts of the refractive index. Here, an average value of m_r = 1.5 is used, based on Atkinson et al. (2015), and absorption is assumed to be negligible. The latter is a reasonable assumption given the relatively high single scatter albedo values at the two sites (Cappa et al., 2016), and because assuming the particles to be slightly absorbing has minimal influence on the results. Temporal variability in m_r due to variability in particle composition will contribute to uncertainty in the retrieved $R_{eff,f}$. As discussed above, a change in m_r of 0.13 corresponds approximately to a shift in $R_{eff,f}$ by 30%. The actual variability in m_r is not known for the particles here, but we expect a shift of 0.13 in m_r to be a reasonable upper limit on physical grounds.

Values of $R_{eff,f}$ are determined using both the CRD-measured b_{ext} and the PM_{10} b_{ext} from the nephelometer + PSAP measurements for both T0 and T1 (Figure 4). $R_{eff,f}$ values are also determined from the PM_1 nephelometer + PSAP measurements at both sites. Comparison of the $R_{eff,f}$ values between the PM_{10} and PM_1 measurements provides a test of the robustness of the overall retrieval method. The $R_{eff,f}$ from the CRD measurements will be referred to as $R_{eff,f,CRD}$ and from the nephelometer + PSAP as $R_{eff,f,sum}$. Comparator values of $R_{eff,f}$ were also calculated from the observed mobility size distributions using Eqn. 1, and are referred to as $R_{eff,f,size}$.

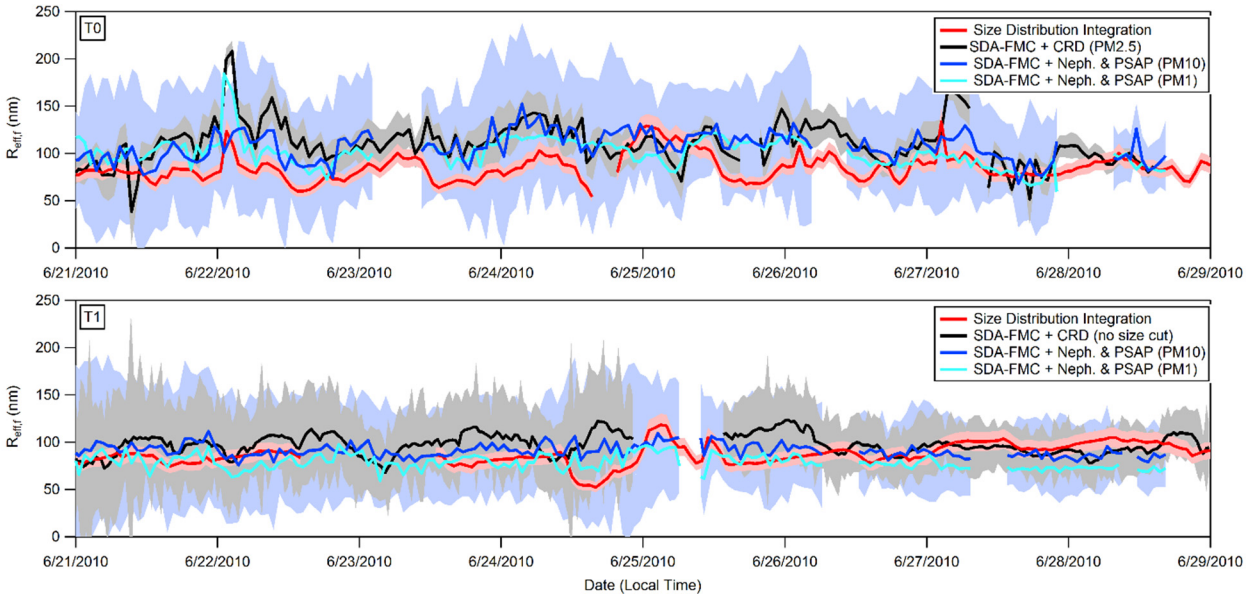

Figure 4 – Time series of the effective fine mode radii, $R_{eff,f}$, produced by the SDA-FMC analysis of the CRD data (black) and the nephelometer + PSAP data (blue) from T0 (top) and T1 (bottom). For the nephelometer + PSAP observations, separate results are shown using either the PM_{10} (dark blue) or PM_1 (light blue) observations. The $R_{eff,f}$ values determined from the size distribution measurements (i.e. from Eqn. 1) are shown in red. Uncertainty ranges are shown as light colored bands for each method; for the SDA-FMC the uncertainty range is only shown for PM_{10} to avoid clutter, but the uncertainty range is similar for PM_1.

The SDA-FMC-derived $R_{eff,f}$ values from the CRD and from the nephelometer + PSAP exhibit reasonably good agreement in terms of the absolute values and the temporal variability at both the T0 and T1 sites (Table 2, Fig. 4). Notably, there is good agreement between the $R_{eff,f,sum}$ values obtained from the PM_{10} and PM_1 measurements. This provides an important validation of the SDA-FMC procedure, since the coarse mode contribution to the PM_{10} extinction is substantial and highly variable (Figure 2 and Figure 3).

At T0, the derived $R_{eff,f}$ values range from approximately 70 nm to 140 nm (Table 2), with a few short-duration periods when $R_{eff,f}$ is outside this range, reflecting short-duration variability in the particle sources. At T1 the derived $R_{eff,f}$ are generally less variable, ranging from approximately 65 nm to 110 nm, with fewer particularly low or high periods. The mean $R_{eff,f}$ values between the two sites are similar (Table 2). At T0, there is a fair degree of temporal coherence of the SDA-FMC results and those obtained from integration of the size distributions. The generally good temporal agreement between the optically- and size-derived $R_{eff,f}$ values are even observed during periods where the changes in radius happened rapidly, for example near midnight between June 21-22. On that night there is some evidence

548 that paving operations near the T0 site produced a strong local source of asphalt particles in the coarse
549 mode with a long tail into the sub-micron regime (Zaveri et al., 2012; Cappa et al., 2016). This short-
550 duration source of large particles pushed the $R_{eff,f}$ temporarily towards larger values. (The $R_{eff,f}$ changes
551 from the nephelometer + PSAP at this time were smaller than from the CRD or size distribution
552 observations. Most likely this reflects the alternating 6-min sampling of the nephelometer and the very
553 short duration of the event leading to discrepancies in the 1 h average.)

554 Despite the generally good correspondence between $R_{eff,f,size}$ and the optically derived values, the $R_{eff,f,size}$
555 values were often (but not always) smaller (Table 2). This is most clearly seen when comparing the
556 average diurnal profiles of the $R_{eff,f}$ values from the different methods, as shown in Figure 5. All three
557 $R_{eff,f}$ estimates exhibit similar diurnal behavior at T0, even though the $R_{eff,f}$ from the SDA-FMC method
558 are larger than $R_{eff,f,size}$. The diurnal variability in the $R_{eff,f}$ is more pronounced at T0 than at T1. The
559 diurnal trend in the effective radius of the fine mode at T0 from all methods exhibits a minimum at
560 around mid-day and then an increase to a maximum right near daybreak. Particle number and sizes at
561 both sites were influenced by frequent regional new particle formation and growth events during CARES
562 (see Figure S2). The events tended to start in the morning with a sharp increase of 10 - 20 nm particles
563 followed by growth of these particles to 50 – 100 nm in the afternoon as discussed in Setyan et al.
564 (2014). The next day the cycle repeats (on average) with the introduction of the new small particles
565 which has the effect of decreasing the average particle radius (Setyan et al., 2014). Although observed at
566 both sites, the new particle formation events had a greater impact on the size distributions at T0,
567 especially in terms of surface area-weighted size distributions (Figure S3) that determine $R_{eff,f}$. In part,
568 this is likely because of continued growth of the new particle mode as it transits from T0 to T1. In
569 addition, for T0 there is a notable mode in the surface-area weighted distribution at ~1 micron that is
570 most evident in the early morning (Figure S3). This mode has little influence on the $R_{eff,f}$ values
571 determined from the size distributions, but contributes to the higher optically determined $R_{eff,f}$ values in
572 the early morning for T0. This mode is much less prevalent at the T1 site, and thus there is better
573 correspondence between the size-distribution and optical methods.

574

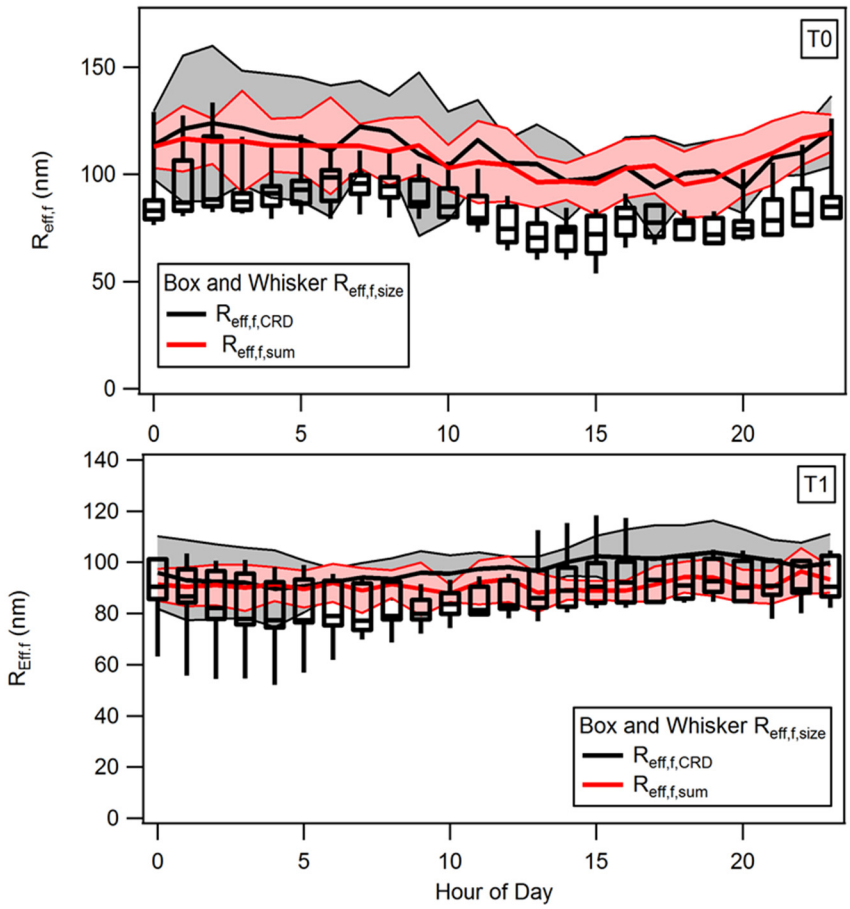

Figure 5 – The diurnal dependence of $R_{eff,f}$ for the period shown in Fig. 4 for the (top) T0 and (bottom) T1 sites. The box and whisker plot (bottom and top of box are 5% and 95% of data range, bar is mean, and whiskers extend to full range) shows the results from the direct size distribution measurement ($R_{eff,f,size}$). The thick lines show the mean diurnal dependence of the optically derived $R_{eff,f}$, using the CRD (black) and nephelometer + PSAP (red) measurements. The light colored bands show the ±1σ standard deviation based on the measurement variability over the averaging period.

One possible explanation for the differences between the optically and size-derived $R_{eff,f}$, in particular at T0, may be inaccurate specification of the refractive index. Temporal variations in or an overall offset of the real refractive index used here from the true value would lead to errors in the optically derived $R_{eff,f}$. The refractive index is used to convert the derived van de Hulst parameter to $R_{eff,f}$ (Eqn. 3). Given the form of the relationship, an absolute error in the real RI of 0.1—likely an upper limit—corresponds to an error in the derived $R_{eff,f}$ of 20%, with larger values of the real RI leading to smaller derived $R_{eff,f}$. The imaginary component was assumed zero. The effective imaginary RI is likely ≤ 0.01, given the range of single scatter albedo values observed (Cappa et al., 2016). Thus, the assumption of zero for the

imaginary RI introduces negligible error. The actual real RI depends on the particle composition since different chemical components (e.g. sulfate, organics, dust) have different RI values. Here, the RI values used were determined based only on measurements of the non-refractory PM composition and only an average value was used (Atkinson et al., 2015). To the extent that refractory components, in particular dust or sea salt, contributed to the fine mode scattering, their influence on the real RI would not be accounted for. However, dust and sea salt contributions are most likely confined primarily to the coarse mode. Thus, the fine mode real refractive index is unlikely to be strongly affected by their presence and the real RI can probably be constrained to a fairly narrow range around 1.5. The relative uncertainty of the $R_{eff,f}$ derived from the SDA-FMC method has been estimated as ranging from 40% to 70%. This range of values was computed from a quadrature combination of the estimated errors (20-50%) in the SDA-FMC retrieval (O'Neill et al., 2003), the CRD measurements (< 5% for the UCD and T0 PSU instrument and 20% for the T1 PSU instrument) and the refractive index term above (estimated maximum of 20%). In this context, the agreement shown in Fig. 4 is acceptable and may suggest that the above error estimates are overly conservative.

Table 2: Summary statistics for $R_{eff,f}$ values (nm) and FMF (unitless fraction)

Site	Method	Maximum		Minimum		Mean		Standard Deviation	
		$R_{eff,f}$ (nm)	FMF	$R_{eff,f}$ (nm)	FMF	$R_{eff,f}$ (nm)	FMF	$R_{eff,f}$ (nm)	FMF
T0	SDA-FMC + CRD ($PM_{2.5}$)	208	0.97	39	0.54	110	0.79	21	0.09
T0	SDA-FMC + Neph. & PSAP (PM_{10})	153	0.85	68	0.35	107	0.62	14	0.12
T0	Size Distribution Integration	133	0.87	54	0.34	85	0.58	14	0.12
T1	SDA-FMC + CRD (no size cut)	176	0.89	46	0.22	102	0.58	18	0.16
T1	SDA-FMC + Neph. & PSAP (PM_{10})	111	0.9	76	0.24	91	0.58	6	0.16
T1	Size Distribution Integration	118	0.87	52	0.24	88	0.61	11	0.15

Conclusions

This work demonstrates that the use of a non-size-selected, three wavelength CRD measurement in continuous field monitoring, coupled with the SDA-FMC analysis, can provide information about the relative contribution of the fine mode to the observed total particle extinction. The retrieved value of the fine mode fraction of extinction is dependent upon the size range of particles sampled and the overall nature of the particle size distribution. The relationship between the FMF_{ext} and the SMF_{ext},

614 determined from near-coincident measurement of extinction by PM_1 and PM_{10}, provides insights into
615 the effective FMF_{ext} split size. For one of the sites considered here the split point size is around 1 μm
616 while for the other it is somewhat larger than 1 μm and perhaps more variable. In many environments,
617 variability in aerosol properties on short (<10 min) timescales is relatively minimal. In such cases, a single
618 instrument can be used to sequentially sample PM_1 and PM_{10}, allowing for *in situ* measurement of both
619 the FMF_{ext} and SMF_{ext}. However, remote sensing measurements characterize only the FMF_{ext}, (or at best,
620 an optically influenced size cut as is done in the AERONET retrievals of Dubovik & King, 2000). Thus,
621 further consideration of *in situ* measurement results, such as those investigated in this study, can
622 provide insights into the interpretation of the FMF_{ext} determined from remote sensing in different
623 environments.

624 The SDA-FMC approach also allows for determination of the effective fine mode radius. The $R_{eff,f}$
625 characterizes the surface-area weighted size of the particles within the fine mode distribution. The
626 similarity of the results in Figure 4 for application of the SDA-FMC to both size-selected and non-size-
627 selected aerosol as well as the comparison with results derived from the PSD measurements verify that
628 "whole air" measurements (i.e., no imposed size-selection) can provide reliable fine mode radii at least
629 for large FMF values.

630 ## Acknowledgements

631 This work was supported by the Atmospheric System Research (ASR) program sponsored by the US
632 Department of Energy (DOE), Office of Biological and Environmental Research (OBER), including Grant
633 No. DE-SC0008937. Funding for data collection was provided by the US DOE's Atmospheric Radiation
634 Measurement (ARM) Program. All data used in this study are available from the ARM data archive at:
635 http://www.arm.gov/campaigns/aaf2009carbonaerosol. The views expressed in this document are
636 solely those of the authors and the funding agencies do not endorse any products or commercial
637 services mentioned in this publication.

Appendix A – Glossary of Symbols and Acronyms used

å	Ångström exponent (from wavelength pair)
α	Spectral derivative of optical property
α’	Curvature (second derivative of optical property in log-log space)
α_f or α'_f	Fine mode version of properties (also coarse mode properties α_c)
AOD	Aerosol optical depth
b_{ext}, b_{scat}, b_{abs}	Optical coefficient for extinction, scattering, absorption (inverse length units)
CRD	Cavity ring down
$R_{eff,s}$	Effective radius for fine mode
FMF (aka η)	Fine mode fraction of an optical property, usually extinction
SMF	Sub-micron fraction (particle mode with radius or diameter smaller than 1 µm)
$\rho_{eff,f}$	Effective fine mode van de Hulst parameter (product of refractive index and effective radius)
SDA	Spectral Deconvolution Algorithm
FMC	Fine Mode Curvature approach
PM_1	Particulate matter with diameter (or radius) smaller than 1 µm (also $PM_{2.5}$, PM_{10})
PSAP	Particle soot absorption photometer instrument

References:

Anderson, T. L., Charlson, R. J., Bellouin, N., Boucher, O., Chin, M., Christopher, S. A., Haywood, J., Kaufman, Y. J., Kinne, S., Ogren, J. A., Remer, L. A., Takemura, T., Tanre, D., Torres, O., Trepte, C. R., Wielicki, B. A., Winker, D. M., and Yu, H. B.: An "A-Train" strategy for quantifying direct climate forcing by anthropogenic aerosols, B. Am. Meteorol. Soc., 86, 1795-1805, doi:10.1175/Bams-86-12-1795, 2005.

Anderson, T. L. and Ogren, J. A.: Determining Aerosol Radiative Properties Using the TSI 3563 Integrating Nephelometer, Aerosol Sci. Technol., 29, 57-69, doi:10.1080/02786829808965551, 1998.

Andrews, E., Sheridan, P. J., Ogren, J. A., and Ferrare, R.: In situ aerosol profiles over the Southern Great Plains cloud and radiation test bed site: 1. Aerosol optical properties, J. Geophys. Res.-Atmos., 109, D06208, doi:10.1029/2003jd004025, 2004.

Ångström, A.: On the atmospheric transmission of sun radiation and on dust in the air, Geografika Ann., 11, 156-166, doi:10.2307/519399, 1929.

Atkinson, D. B., Massoli, P., O'Neill, N. T., Quinn, P. K., Brooks, S. D., and Lefer, B.: Comparison of in situ and columnar aerosol spectral measurements during TexAQS-GoMACCS 2006: testing parameterizations for estimating aerosol fine mode properties, Atmos. Chem. Phys., 10, 51-61, doi:10.5194/acp-10-51-2010, 2010.

Atkinson, D. B., Radney, J. G., Lum, J., Kolesar, K. R., Cziczo, D. J., Pekour, M. S., Zhang, Q., Setyan, A., Zelenyuk, A., and Cappa, C. D.: Aerosol optical hygroscopicity measurements during the 2010 CARES campaign, Atmos. Chem. Phys., 15, 4045-4061, doi:10.5194/acp-15-4045-2015, 2015.

Baibakov, K., O'Neill, N. T., Ivanescu, L., Duck, T. J., Perro, C., Herber, A., Schulz, K. H., and Schrems, O.: Synchronous polar winter starphotometry and lidar measurements at a High Arctic station, Atmos. Meas. Techniq., 8, 3789-3809, doi:10.5194/amt-8-3789-2015, 2015.

Bokoye, A. I., Royer, A., O'Neill, N. T., Cliche, P., Fedosejevs, G., Teillet, P. M., and McArthur, L. J. B.: Characterization of atmospheric aerosols across Canada from a ground-based sunphotometer network: AEROCAN, Atmosphere-Ocean, 39, 429-456, doi:10.1080/07055900.2001.9649687, 2001.

Bond, T. C., Zarzycki, C., Flanner, M. G., and Koch, D. M.: Quantifying immediate radiative forcing by black carbon and organic matter with the Specific Forcing Pulse, Atmos. Chem. Phys., 11, 1505-1525, doi:10.5194/acp-11-1505-2011, 2011.

Brown, S. S.: Absorption Spectroscopy in High-Finesse Cavities for Atmospheric Studies, Chemical Reviews, 103, 5219-5238, doi:10.1021/cr020645c, 2003.

Cappa, C. D., Kolesar, K. R., Zhang, X. L., Atkinson, D. B., Pekour, M. S., Zaveri, R. A., Zelenyuk, A., and Zhang, Q.: Understanding the optical properties of ambient sub- and supermicron particulate matter: results from the CARES 2010 field study in northern California, Atmos. Chem. Phys., 16, 6511-6535, doi:10.5194/acp-16-6511-2016, 2016.

Charlson, R. J., Valero, F. P. J., and Seinfeld, J. H.: In search of balance, Science, 308, 806-807, doi:10.1126/science.1108162, 2005.

692 Clarke, A. and Kapustin, V.: Hemispheric Aerosol Vertical Profiles: Anthropogenic Impacts on Optical
693 Depth and Cloud Nuclei, Science, 329, 1488-1492, doi:10.1126/science.1188838, 2010.

694 Coen, M. C., Andrews, E., Asmi, A., Baltensperger, U., Bukowiecki, N., Day, D., Fiebig, M., Fjaeraa, A. M.,
695 Flentje, H., Hyvarinen, A., Jefferson, A., Jennings, S. G., Kouvarakis, G., Lihavainen, H., Myhre, C. L.,
696 Malm, W. C., Mihapopoulos, N., Molenar, J. V., O'Dowd, C., Ogren, J. A., Schichtel, B. A., Sheridan, P.,
697 Virkkula, A., Weingartner, E., Weller, R., and Laj, P.: Aerosol decadal trends - Part 1: In-situ optical
698 measurements at GAW and IMPROVE stations, Atmos. Chem. Phys., 13, 869-894, doi:10.5194/acp-13-
699 869-2013, 2013.

700 Doran, J. C., Barnard, J. C., Arnott, W. P., Cary, R., Coulter, R., Fast, J. D., Kassianov, E. I., Kleinman, L.,
701 Laulainen, N. S., Martin, T., Paredes-Miranda, G., Pekour, M. S., Shaw, W. J., Smith, D. F., Springston, S.
702 R., and Yu, X. Y.: The T1-T2 study: evolution of aerosol properties downwind of Mexico City, Atmos.
703 Chem. Phys., 7, 1585-1598, doi:10.5194/acp-7-1585-2007, 2007.

704 Dubovik, O. and King, M. D.: A flexible inversion algorithm for retrieval of aerosol optical properties from
705 Sun and sky radiance measurements, J. Geophys. Res.-Atmos., 105, 20673-20696,
706 doi:10.1029/2000jd900282, 2000.

707 Eck, T. F., Holben, B. N., Reid, J. S., Sinyuk, A., Dubovik, O., Smirnov, A., Giles, D., O'Neill, N. T., Tsay, S. C.,
708 Ji, Q., Al Mandoos, A., Khan, M. R., Reid, E. A., Schafer, J. S., Sorokine, M., Newcomb, W., and Slutsker, I.:
709 Spatial and temporal variability of column-integrated aerosol optical properties in the southern Arabian
710 Gulf and United Arab Emirates in summer, J. Geophys. Res.-Atmos., 113, D01204,
711 doi:10.1029/2007jd008944, 2008.

712 Fast, J. D., Gustafson, W. I., Berg, L. K., Shaw, W. J., Pekour, M., Shrivastava, M., Barnard, J. C., Ferrare, R.
713 A., Hostetler, C. A., Hair, J. A., Erickson, M., Jobson, B. T., Flowers, B., Dubey, M. K., Springston, S., Pierce,
714 R. B., Dolislager, L., Pederson, J., and Zaveri, R. A.: Transport and mixing patterns over Central California
715 during the carbonaceous aerosol and radiative effects study (CARES), Atmos. Chem. Phys., 12, 1759-
716 1783, doi:10.5194/acp-12-1759-2012, 2012.

717 George, I. J. and Abbatt, J. P. D.: Heterogeneous oxidation of atmospheric aerosol particles by gas-phase
718 radicals, Nature Chemistry, 2, 713-722, doi:10.1038/nchem.806, 2010.

719 Hamill, P., Giordano, M., Ward, C., Giles, D., and Holben, B.: An AERONET-based aerosol classification
720 using the Mahalanobis distance, Atmos. Environ., 140, 213-233, doi:10.1016/j.atmosenv.2016.06.002,
721 2016.

722 Hansen, J. E. and Travis, L. D.: Light-Scattering in Planetary Atmospheres, Space Sci. Rev., 16, 527-610,
723 doi:10.1007/Bf00168069, 1974.

724 Holben, B. N., Eck, T. F., Slutsker, I., Tanre, D., Buis, J. P., Setzer, A., Vermote, E., Reagan, J. A., Kaufman,
725 Y. J., Nakajima, T., Lavenu, F., Jankowiak, I., and Smirnov, A.: AERONET - A federated instrument network
726 and data archive for aerosol characterization, Remote Sens. Environ., 66, 1-16, doi:10.1016/S0034-
727 4257(98)00031-5, 1998.

728 IPCC: Climate Change 2013: The Physical Science Basis. Contribution of Working Group I to the Fifth
729 Assessment Report of the Intergovernmental Panel on Climate Change, Cambridge University Press,
730 Cambridge, United Kingdom and New York, NY, USA, 2013.

731 Kaku, K. C., Reid, J. S., O'Neill, N. T., Quinn, P. K., Coffman, D. J., and Eck, T. F.: Verification and
732 application of the extended spectral deconvolution algorithm (SDA plus) methodology to estimate
733 aerosol fine and coarse mode extinction coefficients in the marine boundary layer, Atmos. Meas.
734 Techniq., 7, 3399-3412, doi:10.5194/amt-7-3399-2014, 2014.

735 Lack, D. A. and Cappa, C. D.: Impact of brown and clear carbon on light absorption enhancement, single
736 scatter albedo and absorption wavelength dependence of black carbon, Atmos. Chem. Phys., 10, 4207-
737 4220, doi:10.5194/acp-10-4207-2010, 2010.

738 Lack, D. A., Richardson, M. S., Law, D., Langridge, J. M., Cappa, C. D., McLaughlin, R. J., and Murphy, D.
739 M.: Aircraft Instrument for Comprehensive Characterization of Aerosol Optical Properties, Part 2: Black
740 and Brown Carbon Absorption and Absorption Enhancement Measured with Photo Acoustic
741 Spectroscopy, Aerosol Science and Technology, 46, 555-568, doi:10.1080/02786826.2011.645955, 2012.

742 Langridge, J. M., Richardson, M. S., Lack, D., Law, D., and Murphy, D. M.: Aircraft Instrument for
743 Comprehensive Characterization of Aerosol Optical Properties, Part I: Wavelength-Dependent Optical
744 Extinction and Its Relative Humidity Dependence Measured Using Cavity Ringdown Spectroscopy,
745 Aerosol Science and Technology, 45, 1305-1318, doi:10.1080/02786826.2011.592745, 2011.

746 Massoli, P., Bates, T. S., Quinn, P. K., Lack, D. A., Baynard, T., Lerner, B. M., Tucker, S. C., Brioude, J.,
747 Stohl, A., and Williams, E. J.: Aerosol optical and hygroscopic properties during TexAQS-GoMACCS 2006
748 and their impact on aerosol direct radiative forcing, J. Geophys. Res.-Atmos., 114, D00f07,
749 doi:10.1029/2008jd011604, 2009.

750 Moosmuller, H., Chakrabarty, R. K., and Arnott, W. P.: Aerosol light absorption and its measurement: A
751 review, J Quant. Spec. Rad. Trans., 110, 844-878, doi:10.1016/j.jqsrt.2009.02.035, 2009.

752 O'Neill, N. T., Eck, T. F., Holben, B. N., Smirnov, A., Dubovik, O., and Royer, A.: Bimodal size distribution
753 influences on the variation of Angstrom derivatives in spectral and optical depth space, J. Geophys. Res.-
754 Atmos., 106, 9787-9806, doi:10.1029/2000jd900245, 2001.

755 O'Neill, N. T., Eck, T. F., Reid, J. S., Smirnov, A., and Pancrati, O.: Coarse mode optical information
756 retrievable using ultraviolet to short-wave infrared sun photometry: Application to United Arab Emirates
757 unified aerosol experiment data, J. Geophys. Res.-Atmos., 113, D05212, doi:10.1029/2007jd009052,
758 2008a.

759 O'Neill, N. T., Eck, T. F., Smirnov, A., Holben, B. N., and Thulasiraman, S.: Spectral discrimination of
760 coarse and fine mode optical depth, J. Geophys. Res.-Atmos., 108, 4559, doi:10.1029/2002jd002975,
761 2003.

762 O'Neill, N. T., Thulasiraman, S., Eck, T. F., and Reid, J. S.: Robust optical features of fine mode size
763 distributions: Application to the Quebec smoke event of 2002, J. Geophys. Res.-Atmos., 110, D11207,
764 doi:10.1029/2004jd005157, 2005.

765 O'Neill, N. T., Thulasiraman, S., Eck, T. F., and Reid, J. S.: Correction to the effective radius expression in
766 O'Neill et al. (2005), J. Geophys. Res.-Atmos., 113, D24203, doi:10.1029/2008JD011334, 2008b.

767 Ogren, J. A.: Comment on “Calibration and Intercomparison of Filter-Based Measurements of Visible
768 Light Absorption by Aerosols”, Aerosol Sci. Technol., 44, 589-591, doi:10.1080/02786826.2010.482111,
769 2010.

770 Radney, J. G., Bazargan, M. H., Wright, M. E., and Atkinson, D. B.: Laboratory Validation of Aerosol
771 Extinction Coefficient Measurements by a Field-Deployable Pulsed Cavity Ring-Down Transmissometer,
772 Aerosol Science and Technology, 43, 71-80, doi:10.1080/02786820802482536, 2009.

773 Saha, A., O'Neill, N. T., Eloranta, E., Stone, R. S., Eck, T. F., Zidane, S., Daou, D., Lupu, A., Lesins, G.,
774 Shiobara, M., and McArthur, L. J. B.: Pan-Arctic sunphotometry during the ARCTAS-A campaign of April
775 2008, Geophys. Res. Lett., 37, L05803, doi:10.1029/2009gl041375, 2010.

776 Setyan, A., Song, C., Merkel, M., Knighton, W. B., Onasch, T. B., Canagaratna, M. R., Worsnop, D. R.,
777 Wiedensohler, A., Shilling, J. E., and Zhang, Q.: Chemistry of new particle growth in mixed urban and
778 biogenic emissions - insights from CARES, Atmos. Chem. Phys., 14, 6477-6494, doi:10.5194/acp-14-6477-
779 2014, 2014.

780 Setyan, A., Zhang, Q., Merkel, M., Knighton, W. B., Sun, Y., Song, C., Shilling, J. E., Onasch, T. B., Herndon,
781 S. C., Worsnop, D. R., Fast, J. D., Zaveri, R. A., Berg, L. K., Wiedensohler, A., Flowers, B. A., Dubey, M. K.,
782 and Subramanian, R.: Characterization of submicron particles influenced by mixed biogenic and
783 anthropogenic emissions using high-resolution aerosol mass spectrometry: results from CARES, Atmos.
784 Chem. Phys., 12, 8131-8156, doi:10.5194/acp-12-8131-2012, 2012.

785 Smith, J. D. and Atkinson, D. B.: A portable pulsed cavity ring-down transmissometer for measurement
786 of the optical extinction of the atmospheric aerosol, Analyst, 126, 1216-1220, doi:10.1039/B101491,
787 2001.

788 Wiedensohler, A., Birmili, W., Nowak, A., Sonntag, A., Weinhold, K., Merkel, M., Wehner, B., Tuch, T.,
789 Pfeifer, S., Fiebig, M., Fjäraa, A. M., Asmi, E., Sellegri, K., Depuy, R., Venzac, H., Villani, P., Laj, P., Aalto,
790 P., Ogren, J. A., Swietlicki, E., Williams, P., Roldin, P., Quincey, P., Hüglin, C., Fierz-Schmidhauser, R.,
791 Gysel, M., Weingartner, E., Riccobono, F., Santos, S., Grüning, C., Faloon, K., Beddows, D., Harrison, R.,
792 Monahan, C., Jennings, S. G., O'Dowd, C. D., Marinoni, A., Horn, H. G., Keck, L., Jiang, J., Scheckman, J.,
793 McMurry, P. H., Deng, Z., Zhao, C. S., Moerman, M., Henzing, B., de Leeuw, G., Löschau, G., and Bastian,
794 S.: Mobility particle size spectrometers: harmonization of technical standards and data structure to
795 facilitate high quality long-term observations of atmospheric particle number size distributions, Atmos.
796 Meas. Tech., 5, 657-685, doi:10.5194/amt-5-657-2012, 2012.

797 Zaveri, R. A., Shaw, W. J., Cziczo, D. J., Schmid, B., Ferrare, R. A., Alexander, M. L., Alexandrov, M.,
798 Alvarez, R. J., Arnott, W. P., Atkinson, D. B., Baidar, S., Banta, R. M., Barnard, J. C., Beranek, J., Berg, L. K.,
799 Brechtel, F., Brewer, W. A., Cahill, J. F., Cairns, B., Cappa, C. D., Chand, D., China, S., Comstock, J. M.,
800 Dubey, M. K., Easter, R. C., Erickson, M. H., Fast, J. D., Floerchinger, C., Flowers, B. A., Fortner, E.,
801 Gaffney, J. S., Gilles, M. K., Gorkowski, K., Gustafson, W. I., Gyawali, M., Hair, J., Hardesty, R. M.,
802 Harworth, J. W., Herndon, S., Hiranuma, N., Hostetler, C., Hubbe, J. M., Jayne, J. T., Jeong, H., Jobson, B.
803 T., Kassianov, E. I., Kleinman, L. I., Kluzek, C., Knighton, B., Kolesar, K. R., Kuang, C., Kubatova, A.,
804 Langford, A. O., Laskin, A., Laulainen, N., Marchbanks, R. D., Mazzoleni, C., Mei, F., Moffet, R. C., Nelson,
805 D., Obland, M. D., Oetjen, H., Onasch, T. B., Ortega, I., Ottaviani, M., Pekour, M., Prather, K. A., Radney,
806 J. G., Rogers, R. R., Sandberg, S. P., Sedlacek, A., Senff, C. J., Senum, G., Setyan, A., Shilling, J. E.,
807 Shrivastava, M., Song, C., Springston, S. R., Subramanian, R., Suski, K., Tomlinson, J., Volkamer, R.,
808 Wallace, H. W., Wang, J., Weickmann, A. M., Worsnop, D. R., Yu, X. Y., Zelenyuk, A., and Zhang, Q.:

809 Overview of the 2010 Carbonaceous Aerosols and Radiative Effects Study (CARES), Atmos. Chem. Phys.,
810 12, 7647-7687, doi:10.5194/acp-12-7647-2012, 2012.

811

812